RSC Advances

ROYAL SOCIETY OF CHEMISTRY

www.rsc.org/advances

Fracture Toughness and Failure Mechanisms in Un-vulcanized and Dynamically Vulcanized PP/EPDM/MWCNT Blend Nanocomposites

Mehrdad Khodabandelou,[ab] Mir Karim Razavi Aghjeh*[ab] and Majid Mehrabi Mazidi[ab]

[a]Institute of Polymeric Materials, Sahand University of Technology, Sahand New Town, Tabriz, Iran, P.C: 51335-1996

[b]Faculty of Polymer Engineering, Sahand University of Technology Sahand New Town, Tabriz, Iran, P.C: 51335-1996

E-mail: karimrazavi@sut.ac.ir

Abstract

The fracture toughness and deformation mechanisms of un-vulcanized and dynamically vulcanized polypropylene/ethylene-propylene-diene terpolymer (PP/EPDM) blends and polypropylene/ethylene-propylene-diene terpolymer/multi walled carbon nanotube (PP/EPDM/MWCNT) blend-nanocomposites were investigated using the essential work of fracture (EWF) methodology followed by detail microscopy analysis. The effect of maleic anhydride grafted polypropylene (PP-g-MA) on the morphology and fracture toughness of the multicomponent system was also investigated. It was found that both the dynamic vulcanization and compatibilization using PP-g-MA increased the fracture toughness of blend and blend nanocomposite systems. The results illustrated that the dominant fracture mechanism related to the EPDM dispersed phase in un-vulcanized samples was the formation of dilatation bands due to cavitation and/or debonding of dispersed EPDM rubber particles. In vulcanized samples, developing of dilatation shear bands, resulting from repeated particle debonding, was suppressed and the formation of nanovoids and cavitation in rubber particles led to promoting shear yielding of adjacent matrix and dense plastic deformation. Incorporation of MWCNT into the PP/EPDM blend reduced the essential work of fracture (w_e) and enhanced non-essential work of fracture (βw_p). In the blend-nanocomposites, two mechanisms induced by MWCNT were observed. While large MWCNT aggregates acted as favor sites for crack initiation, the individual MWCNT impregnated fibrils arrested the crack propagation. The presence of PP-g-MA diminished negative effect of MWCNT and further enhanced its positive effect through decreasing the size of large aggregates (favor sites to initiate large cracks) and increasing in the number of dispersed individual MWCNT ropes (increase potential of impregnated fibrils formation), respectively.

Keywords: PP/EPDM; Dynamic Vulcanization; MWCNT; Fracture Mechanism; EWF

1. Introduction

Because of notch sensitive nature and poor fracture toughness of polypropylene (PP) on exposure to sever conditions such as low temperature or high deformation rate, the blending of PP with elastomeric polymers such as styrene-ethylene-butylene-styrene (SEBS), ethylene-propylene rubber (EPR) and ethylene-propylene-diene terpolymer (EPDM) is an efficient strategy to increase its toughness.[1-4] Among these rubbers, EPDM is considered as one of the most effective impact modifiers for PP.[3] However, incompatibility of PP and EPDM results in poor interfacial adhesion and consequently unsatisfactory mechanical properties of simple PP/EPDM blends.[5] Mechanical properties of these blends can be improved by using compatibilizers[5-7] and/or dynamic vulcanization process.[7-9] Based on the fact that rubber toughening usually sacrifices the modulus and stiffness of PP, simultaneously reinforcing and toughening of PP is very important to maintain its stiffness-to-toughness balance. The incorporation of micro- and nano-size fillers into PP/elastomer blends can restore the required stiffness and strength. Among the fillers, carbon nanotubes (CNT) in its different types; multi wall carbon nanotubes (MWCNT) and single wall carbon nanotubes (SWCNT) have effective reinforcing effect, because of their large aspect ratio and high tensile strength.[10,11]

The challenges for developing high performance polymer/CNTs nanocomposites include; homogeneous dispersion of CNTs in the polymeric matrix and providing the strong interfacial interactions to ensure efficient load transfer from the polymeric matrix to the CNTs. CNTs are usually present in bundles and exhibit a highly aggregated state in polymeric matrixes because of the strong inter-tube Van Der Waals interactions, which holds the bundles together.[10] Aggregated CNTs could play the role of stress concentrators leading to create the microscopic defects whilst homogeneous dispersion of CNTs prevents the stress concentration and their large surface area provides higher interaction with the polymeric matrix and enhances the stress-transfer mechanisms. Moreover, the fracture strain of CNTs that is estimated to be 10-30%, allows extensive bending and buckling.[12] This high flexibility most probably provides an additional source of high impact strength for the nanocomposites.[13]

The mechanical properties and fracture behavior of PP/CNT nanocomposites have extensively been studied, recently. Prashantha et al.[14] and Zhao et al.[15] reported that PP/MWCNT nanocomposites show ductile behavior in lower loading (1 wt%) and brittle behavior with breaking after the yield point at higher loading (2 wt%). Hemmati et al.[16] reported that the formation of some MWCNT aggregates causes to decrease in tensile and impact strengths of PP/

MWCNTs nanocomposites. Soe et al.[17] showed that the impact strength of PP/MWCNT nanocomposites steadily increases with MWCNT contents at low filler contents and gradually decreases after passing through a maximum with further increasing of the filler content because of CNTs agglomeration. Fracture toughness of PP/MWCNT nanocomposites was studied by Satapathy et al.[18] and they observed higher crack propagation resistance at 0.5 wt% MWCNT nanocomposite compared to pure PP. Prashantha[19] have used PP-g-MA as a compatibilizer to improve the dispersion of CNTs and shown that the Young's modulus, yield stress and impact strength of PP/MWCNT/PP-g-MA nanocomposites are higher than those of PP/MWCNT nanocomposites. Valentini et al.[20] reported that the toughness of PP improved by incorporation of EPDM and it further enhanced by addition of MWCNT. It was also shown by Liu et al. that MWCNT had not a significant effect on the fracture toughness of polypropylene/ethylene-vinyl acetate copolymer (PP/EVA) blend with weight ratio of 80:20, while the impact strength of PP/EVA (60/40) blend greatly increased with MWCNTs.[21]

Our previous research work[7] showed that MWCNT increased the impact strength of un-vulcanized and dynamically vulcanized PP/EPDM (80/20) blends, in which the presence of PP-g-MA had an effective role in increasing the fracture toughness of these blend-nanocomposites. The involved deformation micro-mechanisms were discussed in that work. In this study the fracture behavior of un-vulcanized and dynamically vulcanized PP/EPDM blends and PP/EPDM/MWCNT blend-nanocomposites were investigated using the essential work of fracture method (EWF). The effect of PP-g-MA as a compatibilizer on the toughness of blends and blend-nanocomposites was also investigated. The main focus of this study was to get insight into the micro- and nano-deformation mechanisms induced by different dispersed components which involved in the toughening of such blends and blend-nanocomposites.

2. Experimental

2.1. Materials

Isotactic polypropylene (PP – SI080) with melt flow index of 8.0 g/10 min (230 ºC, 2.16 kg) was obtained from Polynar Petrochemical Company, Tabriz, Iran. EPDM-KEP270 with density of 0.96 g/cm3 (ENB content = 4.5 wt%, ethylene content = 57 wt%) was supplied by Kumho Polychem Company, South Korea. The used multiwall carbon nanotube (MWCNT) was provided by Nanocyl. The specifications of MWCNT are as follow: average diameter 9.5 nm, average length of nanotubes 1.5 μm and purity higher than 90%. The vulcanization ingredients, such as mercaptobenzothiazole disulfide (MBTS), tetramethylthiuram disulfide (TMTD), stearic acid and

sulfur were supplied by Merck. PP-g-MA with MFI value of about 80.0 g/10 min (180ºC/2.16 kg) and 1.2 wt% of grafted maleic anhydride was used in this study.

2.2. Blend preparation

The blends, nanocomposites and blend-nanocomposites were prepared by melt mixing in an internal mixer (Brabender W50EHT) with a 55 ml mixing chamber at starting temperature of 180 ºC and rotor speed of 60 rpm. The chamber was always charged with 45 ml of polymers and mixing was done for 12 min. PP phase (PP or PP+PP-g-MA) was fed into internal mixer followed by the addition of EPDM for un-vulcanized blends and further MWCNT in the melt mixture for un-vulcanized blend-nanocomposites. For different vulcanized samples , 1.5 phr stearic acid and 5 phr zinc oxide were added after 4 min from melt mixing of PP phase with EPDM and MWCNT (for blend-nanocomposites). Then, after 1 min of mixing, accelerators (including 2.1 phr TMTD and 0.9 phr MBTS) were charged and then 1 phr sulfur was added after 30 sec. Typical torque-time curves for un-vulcanized and vulcanized blends together with the blend-nanocomposites are shown in **Fig. 1**. Neat PP and PP phase/MWCNT nanocomposites were also similarly processed for comparison. Prior to the blending, MWCNT and PP-g-MA were dried at 80 ºC under vacuum for 12 h. For all the blends and blend-nanocomposites the weight ratio of PP to EPDM was set at 80:20. For all the nanocomposites and blend-nanocomposites, 0.5 wt% of MWCNT was used. To study the effect of PP-g-MA on MWCNT dispersion and compatibilization of different blends, 2 wt% of PP-g-MA was used in preparation of some samples. To prevent thermo-mechanical degradation during melt blending, 0.1 wt% of thermal stabilizer (Irganox 1010) was used.

Fig. 1

2.3. Instruments

Samples for EWF tests were prepared by compression molding according to ISO 293 and cooled to ambient temperature by water with 15 ± 2 ºC.min-1 average cooling rate. The dimension of EWF test samples was $80 \times 23 \times 1$ mm. The notches were inserted using a sharp razor blade to obtain double edge notched tension (DENT) specimens with a series of ligament length ranging from 13 to 19 mm. At least five specimens were tested for each ligament length and data reduction followed the recommendation of the ESIS-TC4 group.[22] All the fractures for EWF test were performed at room temperature with a crosshead speed of 5 mm/min and using a Zwick/Roell tensile testing machine (Z 010).

To study the morphology and micromechanical deformation processes three preparation and investigation techniques were used:

1) The cryo-fractured surfaces were subjected to pre-treatment to remove the EPDM phase in un-vulcanized samples and also remove the PP phase in vulcanized samples. In un-vulcanized cryo-fractured samples, EPDM phase was etched by cyclohexane at room temperature for 24 h and in vulcanized cryo-fractured samples, PP phase was etched by boiling xylene for 30 sec. The treated samples were then sputter-coated with gold prior to analysis.

2) Single edge notched semi thin films (approximately 40 μm thickness) with dimensions of 80 × 23 mm were prepared by melt-pressing method and inserting notch using sharp razor blade. The prepared film samples were conducted under tensile test with crosshead speed of 5 mm/min and test was terminated when a load of 120 N was reached. Also the un-notched films (same dimensions) were conducted under stress-strain test with a crosshead speed of 5 mm/min until complete failure. In the case of un-notched films, plastically deformed zones close to the fracture plane and for single edge notched films arrested crack-tip damage zone was evaluated by optical microscopy. Although the stress-strain state in semi-thin sections is different from that in bulk material, the nature and mode of deformation cannot be changed and micromechanical deformation mechanisms are comparable in both cases.[23]

3) Morphology of surface and sub-surface of EWF test fractured samples was also investigated. The area of sub-surface interest (marked with arrow in **Fig. 2a**) is perpendicular to the fracture surface and perpendicular to crack growth direction.

Morphology of the fractured surfaces was examined with a HITACHI S-4160 field emission scanning electron microscope (FE-SEM). The deformed and fractured films were studied using an Olympus BX60 optical microscope equipped with a Sony camera (model: SSC-DC58AP).

2.4 Essential work of fracture (EWF) methodology

EWF test method has gained popularity due to its experimental simplicity as the method avoids the measurements of the current crack advance as well as the detection of cracking initiation. EWF concept that proposed first by Broberg[24] and further developed by Cotterell and Reddel[25] and Karger-Kocsis[26-29] has been used extensively to study the fracture behavior of ductile polymeric materials. In this method the total energy required to fracture (W_f) can be divided into the essential work of fracture (W_e) consumed in the inner fracture process zone (IFPZ) to create new surface and non-essential work of fracture (W_p) dissipated in the outer plastic deformation

zone (OPDZ). The related zones are shown schematically in case of a deeply double-edge notched tension specimen in **Fig. 2b**.

Fig. 2

The relationship between work of fracture and its components can be written as follow:

$$W_f = W_e + W_p \qquad (1)$$

By assuming that w_e is proportional to the ligament area, and w_p is proportional to the volume of plastic zone, the relationship between specific terms can be defined as follows:

$$W_f = w_e \times l.t + \beta w_p . \times \ .l^2 .t \qquad (2)$$

$$w_f = w_e + \beta w_p .l \qquad (3)$$

where w_f is the specific total work of fracture, l is the ligament length, t is the thickness of the sample and β is plastic shape factor depending on the geometry of plastic zone.

The total work of fracture, W_f, can be determined by integration of area under force-displacement curves for each specimen. According to Eq. 3, the specific total work of fracture is a linear function of the ligament length. Therefore w_e, that indicates the resistance to crack initiation can be determined from the interception of the linear regression line, fitted to the w_f - l graphs with y-axis and the slope of this line, βw_p, indicates the resistance against crack propagation.

As discussed by Karger-Kocsis et al.[30,31] the total work of fracture can be partitioned at the maximum load as the summation of two contributes: a term W_y related to the yielding of ligament area and another term $W_{n,t}$ associated to the subsequent necking and tearing. Therefore it can be written:

$$W_f = W_y + W_{n,t} \qquad (4)$$

The specific terms (w_y and $w_{n,t}$) can be expressed as a function of ligament length similar to Eq. 2, as follows:

$$w_f = w_y + w_{n,t} = (w_{e,y} + \beta_y w_{p,y} .l) + (w_{e,n,t} + \beta_n w_{p,n,t} .l) \qquad (5)$$

where $w_{e,y}$ is the specific essential yielding-related work of fracture, $w_{e,n,t}$ is the specific essential necking and tearing work, $w_{p,y}$ is volumetric energy dissipated during yielding and $w_{p,n,t}$ is dissipated plastic work during necking and tearing . β_y and $\beta_{n,t}$ are geometry factors related to the shape of the plastic zone during the yielding and necking and tearing, respectively. By comparing Eq. 3 and Eq. 5, it can be concluded that:

$$w_e = w_{e,y} + w_{e,n,t} \quad (6)$$

$$\beta w_p = \beta_y w_{p,y} + \beta_n w_{p,n,t} \quad (7)$$

3. Results and Discussion

3.1 Phase morphology

The SEM micrographs of cryo-fractured surfaces of PP/MWCNT with and without PP-g-MA are shown in **Fig. 3**. It is obvious that the MWCNTs are present in the PP matrix mainly in the form of large aggregates. This indicates imperfect mixing of MWCNT phase in PP matrix. In the presence of PP-g-MA reasonably uniform dispersion and good distribution of the MWCNT with smaller aggregate size was observed. This suggests that the presence of PP-g-MA improves the dispersion state of MWCNT in the PP matrix and limits the formation of MWCNT aggregates.[19]

Fig. 4 shows the SEM images of cryo-fractured surfaces of un-vulcanized PP/EPDM and PP/EPDM/MWCNT with and without PP-g-MA at two different magnifications. The dark holes in the micrographs represent the etched EPDM particles. For the blends and blend-nanocomposites, the matrix-dispersed type phase morphology could be observed. By comparing **Fig. 4a**, **a′** and **Fig. 4b**, **b′** it seems that the incorporation of PP-g-MA into PP/EPDM blend leads to a reduction in the size of dispersed EPDM particles through compatibilization of PP and EPDM phases.[7]

Fig. 3

Fig. 4

It can be seen in **Fig. 4c**, **c′** that the minor EPDM and MWCNT components are mainly separately distributed in the PP matrix in the PP/EPDM/MWCNT blend-nanocomposite sample. Although the addition of PP-g-MA into the PP/EPDM/MWCNT blend-nanocomposite reduced the size of MWCNT aggregates, no obvious effect was observed for the size of dispersed EPDM particles.

The size reduction of MWCNT aggregates due to the presence of PP-g-MA in PP/EPDM/MWCNT sample was also reported in our previous work, as revealed via optical microscopy analysis.[7] By considering that a constant amount of PP-g-MA was used in all the blends and blend-nanocomposites, the less evident effect of PP-g-MA on the EPDM particles in blend-nanocomposite may be related to higher interfacial surface area (PP-EPDM and PP-MWCNT interfaces) in this system than the blend (PP-EPDM interface) which lowers the efficiency of PP-g-MA in decreasing size of EPDM particles in blend-nanocomposites.

The cryo-fractured surfaces of vulcanized samples, did not provide a proper insight into phase morphology (see supporting information), because of agglomeration of EPDM dispersed particles during the etching of PP phase (with boiling xylene for 30 sec). This agglomeration is originated from high surface area of the EPDM dispersed particles and high temperature used for dissolving of the PP matrix. [32]

3.2 Load-displacement curves and EWF parameters

The load-displacement curves of DENT specimens for all the samples during EWF tests are shown in **Fig. 5**. This figure demonstrates that the PP, PP/PP-g-MA and related nanocomposites exhibit brittle-like behavior, without stable crack propagation stage. The trend of load-displacement curves indicates that fast crack propagation takes place in PP and PP/PP-g-MA samples without yielding of the ligament whilst PP/MWCNT and PP/MWCNT/PP-g-MA show a sharp yielding peak, followed by the fast crack propagation and sudden failure. This yielding peak is related to the localized plasticity at the roots of pre-cracks of the EWF test specimens.

In the case of un-vulcanized and vulcanized blends as well as blend-nanocomposites, well developed crack initiation and crack propagation regions are observed on the load-displacement curves. The load reached a maximum, as a definite yield point occurred, and after the peak, the load dropped steadily until failure of the specimen. This trend is characteristic of ductile fracture behavior as the ligament fully yields and the crack propagates in a stable manner.

Fig. 5 also indicates that the presence of MWCNTs in PP/EPDM blends causes some instability during the crack propagation stage of both un-vulcanized and vulcanized systems. These instabilities are believed to be due to nonhomogeneous dispersion of MWCNTs and presence of carbon nanotube aggregates in the matrix.[33] It is also obvious from **Fig. 5** that the addition of PP-g-MA into different blend-nanocomposites, diminished the level of instability

during the fracture process. This may be attributed to the size reduction of MWCNT aggregates due to the presence of PP-g-MA as discussed earlier and reported in our previous work.[7]

The load-displacement curves for all the blends and blend-nanocomposits show that shape of the curves remains the same as the ligament length increases. This is one of the most important prerequisites of EWF test method and indicates that the crack propagates in the same manner for different ligament lengths, and fracture mode of the test sample being unchanged with the ligament length. To ensure that the EWF data were obtained under plane stress conditions for the blends and blend-nanocomposits, and to remove data where fracture occurred prior to full ligament yielding, net-section stress at maximum σ_{max} ($\sigma_{max} = F_{max} / lt$, where F_{max} is the maximum load in the load-displacement curves) was calculated for different ligament lengths and plotted against ligament length for different samples (**Fig. 6**). Accordingly, an average value of maximum stress (σ_{mean}) was calculated and the results are assumed to be valid if the maximum stress is within the range of 0.9-1.1 σ_{mean}.

Fig. 5

Fig. 6 clearly shows that the data for all the blends and their nanocomposites lie within the range of $0.9\sigma_{mean}$ and $1.1\sigma_{mean}$, indicating that the EWF tests have been conducted under plane stress conditions recommended by ESIS protocol.[22] Other important prerequisite of EWF test method is that the plastic zone has not spread over the lateral boundaries of the specimens.

Fig. 6

According to **Fig. 7**, there is no evidence for spreading of yielded zones to lateral boundaries of the EWF test samples. The above mentioned criteria confirm the applicability of EWF test method to the blends and blend-nanocomposites with ductile fracture behavior in this work and also the validity of the obtained data.

Fig. 7

It should be noted that lack of prerequisites of EWF test method invalidates the use of this approach for evaluation fracture toughness of PP, PP/PP-g-MA and related nanocomposites that display unstable crack propagation. Although the fracture energies obtained for these samples are

apparent values and not the intrinsic properties, the crack resistance of these materials was determined by the EWF methodology to provide a qualitative comparison with those calculated for ductile samples.[34]

The values of w_e and βw_p for PP, PP/PP-g-MA and their nanocomposites obtained from the interception extrapolated to zero ligament length and slope of the straight lines, respectively, are listed in **Table I**. The results of **Table I** indicates that almost total fracture energy of PP, PP/PP-g-MA, PP/MWCNT and PP/MWCNT /PP-g-MA samples is dissipated in the inner region near the fracture surface (w_e) and a negligible energy is dissipated in the outer plastic zone (βw_p). The results also show that addition of PP-g-MA into PP reduced the w_e and βw_p values. Although the extent of reduction is low, it could be attributed to the poor mechanical properties of PP-g-MA relative to the PP, owing to its lower molecular weight. On the other hand, incorporation of MWCNT increased the w_e and βw_p values and these parameters further increased by addition of PP-g-MA into PP/MWCNT nanocomposites. While the dominant fracture mechanism in these brittle-like samples seems to be the crazing, the increased w_e and βw_p values of MWCNT filled nanocomposites may be due to the nucleation of multiple crazing promoted by MWCNT aggregates. It should be noted that MWCNTs (nanotube ropes and nanotube aggregates) reduce the spherulite size of PP through act as nucleating agent.[35] This lead to smaller inter-spherulitic boundary that is favor to crack initiation sites and also could allow the matrix to deform easier with notice that polymers with larger spherulites tend to be more embrittle.[36] Therefore, promoting multiple crazing and reduction of spherulite size could be responsible for increased fracture toughness of PP-based nanocomposites as compared with pure PP, which in turn led to yielding of the material at the notch tip. The slight increase in the work of fracture parameters of PP/MWCNT upon the addition of PP-g-MA could be attributed to the better dispersion of MWCNTs in the matrix, which was discussed in the "phase morphology" section.

Table I

A summary of the values of w_e and βw_p parameters together with the results for splitting the essential and non-essential work of fracture into yielding and necking terms for different blends and blend-nanocomposites, obtained by plotting w_y-l and w_n-l, are listed in **Table II**.

Comparing the results of **Table II** with those of **Table I** shows that incorporation of 20 wt % EPDM into PP increased the w_e and βw_p parameters simultaneously, as expected. This is

attributed to the toughening mechanisms such as internal void formation, matrix shear yielding and/or interfacial debonding related to the dispersed rubber particles. The addition of PP-g-MA enhanced the essential and non-essential works of fracture of PP/EPDM blend, contrary to pure PP. Compatibilization effect of PP-g-MA in PP/EPDM blend with subsequent improvement in interfacial adhesion between PP and EPDM phases could be the main reason for increased fracture toughness of PP/EPDM/PP-g-MA blend. The compatibilization role of PP-g-MA has been reported in the literature[6,7] and also was confirmed in previous section.

Table II

According to the results of **Table II**, it is obvious that the incorporation of MWCNT into un-vulcanized PP/EPDM blend reduced the w_e value along with an increase in βw_p. Similar to PP/EPDM blend, the presence of PP-g-MA in un-vulcanized PP/EPDM/MWCNT nanocomposite, increased both the w_e and βw_p values. However, the extent of improvement in the w_e value for un-vulcanized PP/EPDM blend upon the introduction of PP-g-MA is much higher than that obtained by addition of PP-g-MA into its blend-nanocomosite counterpart. This might be due to the fact that in the compatibilized PP/EPDM/MWCNT blend-nanocomposite, the PP-g-MA distributes at the interfacial region between both the dispersed components (MWCNT and EPDM) and the matrix which could reduce its effective concentration at the PP/EPDM interface as compared to the unfilled PP/EPDM binary blend.

The data in **Table II** show that the dynamic vulcanization greatly improved the specific EWF and specific plastic work values of the blends and blend-nanocomposites, so that the vulcanized samples exhibited significantly higher work of fracture parameters than their un-vulcanized counterparts. This is primarily due to the fact that vulcanization process improves the interfacial interaction between PP and EPDM phases and also increases the cohesive strength of EPDM rubber particles. Similar to un-vulcanized samples, the presence of MWCNTs in vulcanized PP/EPDM blends (with and without PP-g-MA) decreased the w_e value and increased βw_p parameter. The reason behind of these variations and involved micro-mechanisms will be more evidenced by splitting the different terms as appeared below.

3.3 constituting terms of essential and non-essential work of fracture

In the case of neat PP and PP-based samples with brittle-like fracture behavior, the w_e and βw_p values reported in **Table I** are almost entirely consumed during the yielding up to crack initiation stage of the fracture process ($w_e \approx w_{e,y}$ and $\beta w_p \approx \beta_y w_{p,y}$) with negligible contribution from the crack propagation stage ($w_{e,n,t} \approx 0$ and $\beta_n w_{p,n,t} \approx 0$), as expected. But for un-vulcanized and vulcanized blends and blend-nanocomposites which behaved in ductile manner with stable crack propagation, it is apparent that the contribution made by necking and tearing stage is much greater than that of yielding stage for both w_e and βw_p parameters, as measured and recorded in **Table II**. This is characteristic of completely stable crack propagation in these samples. Very interesting results can be observed at the first look to the **Table II**. Presence of PP-g-MA significantly increased energy dissipation during necking and tearing stage ($w_{e,n,t}$) of the fracture process for blends and blend-nanocomposites, especially for un-vulcanized samples. The results of **Table II** also demonstrate that in one hand un-vulcanized and vulcanized PP/EPDM/MWCNT blend-nanocomposites have higher $w_{e,y}$ and lower $w_{e,n}$ than un-vulcanized and vulcanized PP/EPDM blends, respectively, and on the other hand incorporation of PP-g-MA into un-vulcanized and vulcanized PP/EPDM/MWCNT blend-nanocomposites increases both $w_{e,y}$ and $w_{e,n}$. Moreover by considering that the presence of MWCNTs have negative effect on the fracture toughness (w_e) of un-vulcanized and vulcanized PP/EPDM samples (with and without PP-g-MA), it may be concluded that MWCNT aggregates facilitate tearing process, while the presence of PP-g-MA due to reduction in the size of MWCNT aggregates increases the resistance to tearing and crack propagation. Overally, the results of **Table II** show that the fracture toughness of all the samples is controlled by necking and tearing components of work of fracture. These will be more evidenced and discussed using detail fractography studies in the next section.

3.4 Toughening and failure mechanisms

SEM images of PP, PP/PP-g-MA, PP/MWCNT and PP/MWCNT/PP-g-MA fractured surfaces under EWF test conditions are depicted in **Fig. 8**. Smooth fractured surfaces without shear yielding and/or plastically deformed materials imply that little energy is dissipated during fracture process of these samples (**Fig. 8 a-d**). These morphologies confirm the brittle-like failure behavior of PP, PP/PP-g-MA, PP/MWCNT and PP/MWCNT /PP-g-MA samples with low fracture toughness.

As stated before, the presence of MWCNTs not only reduces the size of spherulites of the PP matrix[36], but also MWCNT aggregates could serve as the sites for the initiation of craze-like features throughout the PP-based nanocomposites. Moreover, the MWCNT aggregates could act as crack deviation and therefore could change the direction of crack growth. These mechanisms were also reported for halloysite nanotubes filled PA6.[37] The toughening mechanisms, induced by MWCNTs in PP/MWCNT nanocomposite, are demonstrated in **Fig. 9**. Optical microphotograph of PP/MWCNT nanocomposite shows that MWCNT aggregates act as both craze initiation sites **(Fig. 9 a**) and crack deviation (**Fig. 9 b**).

Fig. 8

Fig. 9

Optical microscopy images of deformation zones developed ahead of the arrested crack tip of SEN films for PP, un-vulcanized and vulcanized PP/EPDM blends are shown in **Fig. 10**. These microphotographs were obtained by transmission optical microscopy (TOM) in the bright-field mode, so the voided materials appear dark in the micrographs. Little deformation surrounding the crack tip of PP sample is observed in **Fig. 10a**. This image indicates that the crack-tip plastic zone of PP consists mainly of small number of long micro-cracks. When the plastic zone reaches to a critical size and fulfils the unstable condition of the deformation, the macro-crack develops and the brittle fracture takes place.

In contrary with PP, the crack-tip damage zone of un-vulcanized PP/EPDM blend **(Fig. 10b**) is composed of a large number of dilatation band features, so that a large damage zone has been developed in front of the crack tip. It is believed that the dilatation bands are formed by sequential (repetitive) cavitation and/or debonding of dispersed EPDM rubber particles.[2,38] The presence of EPDM particles leads to relaxation of the stress concentration due to the release of strain constraint by internal void formation of EPDM particles and/or interfacial debonding from the surrounding matrix. Therefore, the nucleation of catastrophic crack is suppressed and the fracture toughness (w_e) is improved as compared with pure PP.

It is clearly visible in **Fig. 10c** that dynamic vulcanization further intensifies the different deformation processes in front of crack-tip. As can be seen, larger crack-tip damage zone composed of a much more dense-bundle of dilatation bands are developed in ahead of crack tip for vulcanized PP/EPDM blend as compared to un-vulcanized blend. It seems that a larger number of bands with much lower thicknesses have been developed in vulcanized blend.

Moreover, the vulcanized PP/EPDM blend showed a large crack-tip yielded zone at the close proximity of the pre-crack, visible as a dark dog-bone region which is absent in the un-vulcanized PP/EPDM blend. Therefore, larger volume of the material participates in energy absorption and/or dissipation processes in vulcanized sample than the un-vulcanized sample, which results in a greatly improved fracture toughness of vulcanized blend.

Fig. 10

Fig. 11 shows optical microscopy image taken from sub-surface damaged zones of un-notched films along with SEM image taken from sub-surface of EWF fractured sample, for un-vulcanized and vulcanized PP/EPDM blends. **Fig. 11a** shows dilatation bands in sub-surface deformed zone which is apparently constituted of a row of cavitated and/or debonded rubber particles. It is clear from this image that the extent of deformation decreases when moving away from the fractured surface in the specimen. The formation of these bands confirms the hypothesis of a limited adhesion between PP and dispersed EPDM particles. During the band propagation, the ligaments of polymer between micro-voids are allowed to deform and stretch. This plastic deformation and stretching of the ligaments is actually the real source of toughness associated with the formation of dilatational shear bands[38] and is responsible for higher toughness of un-vulcanized PP/EPDM blend than the neat PP. **Fig. 11b** also shows some elongated voids formed due to the formation of internal cavities in the rubber particles and/or debonding at the interface of PP and EPDM particles. It can interestingly be seen in this figure that the cavities are arranged preferentially along a straight line. This is accordance with the results of optical microscopy (**Fig. 11a**) and emphasizes again that the deformation mechanism in un-vulcanized PP/EPDM blend is massive dilatation shear banding. Similar mechanisms were reported by Zebarjad for simple PP/EPR (80/20) blend.[2,38,39]

Fig. 11

It can be seen from **Fig. 11c** and **d** that the size of voids has decreased in vulcanized blend compared with un-vulcanized blend. This could be related to the improved cohesive energy of EPDM particles and also interfacial adhesion of PP and EPDM phase due to vulcanization process.[9] However, nanovoids formation and cavitation in rubber particles could lead to promoting shear yielding and plastic deformation of adjacent matrix material. Dense and extensive damage zone of vulcanized blend indicates severe deformation in this area in comparison with un-vulcanized blend. Therefore one could claim that in vulcanized blend, because of improved interfacial adhesion between PP and EPDM phases, developing of dilatation

shear bands through repeated particle debonding is suppressed and here it seems that the main mechanism is shear yielding of PP matrix. This is also evident from more developed stress whitening effects observed ahead of the arrested crack tip of vulcanized sample than un-vulcanized one (**Fig. 10c** and see also Fig. 7a and b).

Fig. 12 shows SEM images of fractured surfaces of un-vulcanized and vulcanized PP/EPDM blends with and without PP-g-MA, under EWF test at two magnifications. As shown in this figure, plastic deformation and stretching of the matrix ligaments followed by necking and twisting are the dominant deformation mechanisms of these samples. Shear-induced size reduction during vulcanization, [40] and also improved interfacial adhesion between PP and dispersed EPDM phase along with more resistive EPDM particles against tearing for vulcanized samples compared with un-vulcanized ones greatly increase the resistance to crack initiation and subsequent crack propagation in the form of larger w_e and $w_{e,n,t}$ values for former system than the latter one (**Table II**). The above mentioned difference in the deformational micro-mechanisms of un-vulcanized and vulcanized PP/EPDM blends cause a different fracture pattern on the surface of deformed samples, as can be seen in **Fig. 12.**

It is relatively hard to differentiate in fracture mechanisms that occurred in samples with and without PP-g-MA based on the micrographs in **Fig. 12.** However, higher fracture toughness of PP/EPDM/PP-g-MA compared with PP/EPDM blend is probably due to higher interfacial adhesion between PP and EPDM phase in the former blend than the latter one.

Optical microscopy images of deformation zones developed ahead of the arrested crack tip for un-vulcanized and vulcanized PP/EPDM/MWCNT blend-nanocomposites are shown in **Fig. 13**. Similar to un-filled samples, vulcanization caused to an intensified and large damage zone in front of crack tip of MWCNT filled blend. **Fig. 13** reveals that MWCNT aggregates act as stress concentrator sites, so that large MWCNT aggregates located in highly deformed zone are debonded from the matrix (shown by arrows). Therefore, large MWCNT aggregates could have main role in unstable crack growth through crack nucleation in weakened zones caused by debonding from matrix.

Fig. 12

Fig. 13

The SEM micrographs taken from the EWF test fractured surfaces of different blend-nanocomposites are shown in **Fig. 14**. The low magnification micrographs of MWCNT filled samples display less disturbed surfaces as compared with un-filled samples (**Fig. 12**). This is probably due to hindrance of fibril yielding process imposed by MWCNT. Similar observation

has been reported for PP-based nanocomposite containing 0.5 wt% MWCNT.[12] This process manifests itself in the form of a larger yielding-related specific work of fracture ($w_{e,y}$) for all the blend-nanocomposites than their un-filled counterparts, as depicted in the results of **Table II**.

Fig. 14

Decrement of w_e and increment of βw_p for un-vulcanized and vulcanized blend-nanocomposites compared with un-vulcanized and vulcanized blends, respectively, could be related to two different micro- and nano-mechanisms induced by MWCNTs: From one hand, the large sized MWCNT aggregates act as crack initiation sites which reduce the crack initiation resistance of the material (**Fig. 15 a, b**) and on the other hand, developing the individual MWCNT impregnated fibrils, those have high strength, arrest the crack propagation (**Fig. 15 a, c**). The former micro-mechanism leads to a decrease of w_e (term related to resistance to crack initiation) while the latter nano-mechanism leads to an increase in βw_p (term related to resistance to crack propagation) through blocking the growing voids. It should be noted that this type of crack propagation is irregular, which is evident from waviness in load-displacement curves of blend-nanocompostes during the crack propagation stage (**Fig. 5**). Arresting of the crack propagation by nanoclay impregnated fibrils has been reported by Saminathan.[41]

Fig. 15

With notice to the above discussed micro- and nano-mechanisms, it is reasonable that the PP-g-MA increase both the w_e and βw_p parameters of the blend-nanocomposites through decrease the size of large aggregates (favor sites to initiate large crack) and increase in the number of dispersed individual MWCNT ropes. On the other hand, the results of **Table II** indicate that $w_{e,n}$ decreases in the presence of MWCNT. This suggests, despite the presence of the MWCNT impregnated fibrils that potentially could have the main role in increment of tear resistance of the sample, the MWCNT aggregates act as defect and facilitate tearing process.

It is worth to note that since in PP-based nanocomposites the dominant fracture mechanism is crazing, the MWCNT aggregates increase the fracture toughness of the resulting materials, through acting as nucleation sites for crazes/micro-cracks, whereas in blend-nanocomposites, with shear banding followed by shear yielding as the main source of energy dissipation, the presence of MWCNT aggregates has a negative impact on the fracture toughness of the resulting systems.

Fig. 16 shows SEM images of sub-surface for the un-vulcanized PP/EPDM/MWCNT blend-nanocomposite sample, fractured in EWF test. According to this figure, it can be concluded that the presence of MWCNTs in un-vulcanized PP/EPDM blend has not changed the nature of micro-mechanisms of deformations related to EPDM particles and also dilatation shear banding occurs in un-vulcanized blend-nanocomposites similar to unfilled counterpart.

Fig. 16

4. Conclusions

Fracture behavior and deformation mechanisms of MWCNT filled PP/EPDM blends were studied using the EWF methodology and evidenced using detail electron and optical microscopy analysis. The results showed that dynamic vulcanization as well as addition of PP-g-MA improved the essential and plastic work of fracture of PP/EPDM blends and PP/EPDM/MWCNT blend-nanocomposites. The results illustrated that the main fracture mechanism in un-vulcanized samples was the formation of dilatation bands, while in vulcanized samples, developing of dilatation shear bands due to repeated debonding was suppressed and in these samples formation of nano-scale voids in rubber particles led to promoting shear yielding of adjacent matrix and dense plastic.

In the blend-nanocomposites, two conflicting MWCNT induced mechanisms were observed: large MWCNT aggregates acted as favor sites for crack initiation that led to a decrease of w_e and on the other hand individual MWCNT impregnated fibrils arrested the crack propagation that coused an increase in βw_p through blocking the growing voids. In this case, PP-g-MA displayed a beneficial role on the fracture toughness of the blend-nanocomposites. The energy-partitioning approach revealed an increase in both energy consumed for yielding ($w_{e,y}$) and energy dissipated during ductile tearing ($w_{e,n}$) of the compatibilized systems compared with uncompatibilized ones.

Associated content (Supporting information)

The SEM micrographs from cryofractured surface of vulcanized PP/EPDM in different magnifications are given in the Supporting information, Fig. S1.

References

1 A. K. Gupta and, S. N. Purwar, *J. Appl. Polym. Sci*., 1986, **31**, 535–551.

2 S.M. Zebarjad, A. Lazzeri, R. Bagheri, S.M. Seyed Reihani, M. Frounchi, *Mater. Lett*., 2003, **57**,2733– 2741.

3 X-G. Tang, R-Y. Bao, W. Yang, B-h. Xie, M-bo. Yang, M. Hou, *Europ. Polym. J*., 2009, **45**, 1448–1453.

4 F. Chen, B. Qiu, B. Wang, Y. Shangguan and Q. Zheng, *RSC Adv*., 2015, **5**, 20831-20837.

5 B. C. Kim, S. S. Hwang, K. Y. Lim, K. J. Yoon, *J. Appl. Polym. Sci*., 2000, **78**, 1267–1274.

6 I. Hejazi, F. Sharif, H. Garmabi, *Mater. Des.* 2011, **32**, 3803–3809.

7 M. khodabandelou, M. K. Razavi Aghjeh, *Polym. Bull*. 2015 (submitted and is in the revision process).

8 N. K. Gupta, A. K. Jain, R. Singhal and A. K. Nagpal, *J. Appl. Polym. Sci*., 2000, **78**, 2104–2121.

9 M. Ishikawa, M. Sugimoto, T. Inoune, *J. Appl. Polym. Sci*., 1996, **62**, 495–1502.

10 J. Huang, D. Rodrigue, *Mater. Des.* 2015, **65**, 974–982.

11 E. Logakis, E. Pollatos, Ch. Pandis, V. Peoglos, I. Zuburtikudis, CG. Delides, A. Vatalis, M. Gjoka, E. Syskakis, K. Viras, P. Pissis, *Comp. Sci. Technol*., 2010, **70**, 328–335.

12 M. Ganß, B. K. Satapathy, M. Thunga, R. Weidisch, P. Potschke, D. Jehnichen, *Acta. Mater*., 2008, **56**, 2247–2261.

13 D. Bikiaris, *Materials*, 2010, **3**, 2884-2946.

14 K. Prashantha, J. Soulestin, M.F. Lacrampe, P. Krawczak, G. Dupin, M. Claes, *Comp. Sci. Technol*., 2009, **69**, 1756–1763.

15 P. Zhao, K. Wang, H. Yang, Q. Zhang, R. Du, Q. Fu, *Polymer* ,2007, **48**, 5688-5695.

16 M. Hemmati, G. H. Rahimi, A. B. Kaganj, S. Sepehri & A. M. Rashid, *J. Macromol. Sci., Part B: Physics*, 2008, **47**, 1176–1187.

17 M-K. Seo, J-R. Lee, S-J. Park, Mater. *Sci. and Engin*., 2005, **404**, 79–84.

18 B. K. Satapathy, M. Ganß, R. Weidisch, P. Po¨tschke, D. Jehnichen, T. Keller, K. D. Jandt, Macromol. *Rapid Commun*. 2007, **28**, 834–841.

19 K. Prashantha, J. Soulestin, M. F. Lacrampe, M. Claes, G. Dupin, P. Krawczak, *Expr. Polym. Lett*., 2008, **2**, 735–745.

20 L. Valentini, J. Biagiotti, M. Kenny, M.A.L Manchado*, J. Appl. Polym. Sci*., 2003, **89**, 2657-2663.

21 L. Liu, Y. Wang, Y. Li, J. Wu, Z. Zhou, C. Jiang, *Polymer*, 2009, **50**, 3072-3078.

22 E. Clutton, D.R. Moore, A. Pavan, J.G. Williams, editors. *Elsevier Science Ltd*, 2001, 177–195.

23 G-M. Kim, G. H. Michler, *J. Appl. Polym. Sci*. 1996, **60**, 1391–1403.

24 K. B. Broberg, *Int. J. Fract*., 1968, **4**, 11-18.

25 B. Cotterell and J. K. Reddel, *Int. J. Fract*., 1977, **13**, 267-277.

26 J. Karger-Kocsis, E. J. Moskala, *Polym. Bull*., 1997, **39**, 503-510.

27 J. Karger-Kocsis, T. czigany and E. J. Moskala, *Polymer*, 1997, **38**, 4587-4593.

28 J. Karger-Kocsis, *Polym. Bull.*, 1996, **37**, 119-126.

29 T. Barany, J. Karger-Kocsis, T. Czigany, *J. Polym. Degrad. Stab*., 2003, **82**, 271-278.

30 D. E. Mouzakis, J. Karger-Kocsis and E. J. Moskala, *J. Mater. Sci. Lett*., 2000, **19**, 1615-1619.

31 J. Karger-Kocsis, D. Ferrer-Balas, *Polym. Bull*., 2001, **46**, 507-512.

32 C. Yukun, X. Chuanhui, C. Liming, W. Yanpeng, C. Xiaodong*, Polym. Test*., 2012, **31**, 728–736.

33 J. Karger-Kocsis, V.M. Khumalo, T. Bárány, L. Mészáros and A. Pegoretti, *Compos. Interf*., 2013, **20**, 395–404.

34 M. Mehrabi Mazidi and M. K. Razavi Aghjeh, *RSC Adv*., 2015, **5**, 47183-47198.

35 A. R. Bhattacharyya, T. V. Sreekumar, T. Liu, S. Kumar, L. M. Ericson, R. H. Hauge, R. Smalley, *Polymer*, 2003, **44**, 2373–2377.

36 H. Zhang, Z. Zhang, *Europ. Polym. J*., 2007, **43**, 3197-3207.

37 K. Prashantha, , H. Schmitt, M.F. Lacrampe, P. Krawczak, *Compos. Sci. and Tech*., 2011, **71**, 1859–1866.

38 S. M. Zebarjad, R. Bagheri, A. Lazzeri, S. Serajzadeh, *Mater. Des*. , 2004, **25**, 247–250.

39 S. M. Zebarjad, R. Bagheri, S. M. Seyed Reihani, A. Lazzeri*, J. Appl. Polym. Sci*., 2003, **90**, 3767–3779.

40 A. K. Jain, A. K. Nagpal, R. Singhal and Neeraj K. Gupta, *J. Appl. Polym. Sci*., 2000 ,**78**, 2089–2103.

41 K. Saminathan, P. Selvakumar, N. Bhatnagar, *Polym. Test*., 2008, **27**,453–458.

Figure captions

Fig. 1: Schematic mixing torque-time diagrams of un-vulcanized blend and blend nanocomposite (**a** and **b**) and vulcanized blend and blend nanocomposite (**c** and **d**).

Fig. 2: **a**) Locations inside the plastic deformation zone that observed by scanning electron microscopy, **b**) Deeply double-edge notched specimen and the different energy dissipation zones involved.

Fig. 3: SEM micrographs of **a**) PP/MWCNT, **b**) PP/MWCNT/PP-g-MA. MWCNT aggregates are shown by arrows.

Fig. 4: SEM micrographs of different samples. **a**,**a′**) un-vulcanized PP/EPDM, **b**,**b′**) un-vulcanized PP/EPDM/PP-g-MA, **c**,**c′**) un-vulcanized PP/EPDM/MWCNT and **d**,**d′**) un-vulcanized PP/EPDM/PP-g-MA/MWCNT. The EPDM phase was etched by cyclohexane.

Fig. 5: Load-displacement curves of DENT specimens with different ligament lengths in EWF tests. **a**) PP, **b**) PP/PP-g-MA, **c**) PP/MWCNT, **d**) PP/PP-g-MA/MWCNT, **e**) un-vulcanized PP/EPDM, **f**) vulcanized PP/EPDM, **g**) un-vulcanized PP/EPDM/PP-g-MA, **h**) vulcanized PP/EPDM/PP-g-MA, **i**) un-vulcanized PP/EPDM/MWCNT, **j**) vulcanized PP/EPDM/MWCNT, **k**) un-vulcanized PP/EPDM/PP-g-MA/MWCNT and **l**) vulcanized PP/EPDM/PP-g-MA/MWCNT.

Fig. 6: maximum stress (σ_{max}) against ligament length for **a**) un-vulcanized PP/EPDM, **b**) vulcanized PP/EPDM, **c**) un-vulcanized PP/EPDM/PP-g-MA, **d**) vulcanized PP/EPDM/PP-g-MA, **e**) un-vulcanized PP/EPDM/MWCNT, **f**) vulcanized PP/EPDM/MWCNT, **g**) un-vulcanized PP/EPDM/PP-g-MA/MWCNT and **h**) vulcanized PP/EPDM/PP-g-MA/MWCNT.

Fig. 7: Fractured DENT samples under EWF test. **a**) un-vulcanized PP/EPDM, **b**) vulcanized PP/EPDM, **c**) un-vulcanized PP/EPDM/PP-g-MA, **d**) vulcanized PP/EPDM/PP-g-MA, **e**) un-vulcanized PP/EPDM/MWCNT, **f**) vulcanized PP/EPDM/MWCNT, **g**) un-vulcanized PP/EPDM/PP-g-MA/MWCN and **h**) vulcanized PP/EPDM/PP-g-MA/MWCNT.

Fig. 8: SEM micrographs of the fracture surface of EWF-test specimens. **a**) PP, **b**) PP/PP-g-MA, **c**) PP/MWCNT and **d**) PP/MWCNT /PP-g-MA**.**

Fig. 9: Optical photomicrograph of PP/MWCNT, **a**) MWCNT aggregate act as craze initiation site, **b**) MWCNT aggregate act as crack patch hindering. The black arrows in (b) show crack path.

Fig. 10: Optical microscopy images of deformation zones that developed ahead of the arrested crack tip. **a**) PP, **b**) un-vulcanized PP/EPDM and **c**) vulcanized PP/EPDM.

Fig. 11: Optical microscopy images of sub-surface damaged zones for un-notched films (**a**, **c**) and SEM micrographs taken from sub-surface region of EWF-test specimen (**b**, **d**). Un-vulcanized PP/EPDM (**a**, **b**) and vulcanized PP/EPDM (**c**, **d**).

Fig. 12: SEM micrographs of the fracture surface of EWF-test specimens. **a**, **a′**) un-vulcanized PP/EPDM, **b**, **b′**) vulcanized PP/EPDM and **c**, **c′**) un-vulcanized PP/EPDM/PP-g-MA and **d**, **d′**) vulcanized PP/EPDM/PP-g-MA under EWF test at two magnifications.

Fig. 13: Optical microscopy images of deformation zones that developed ahead of the arrested crack tip. **a**) un-vulcanized PP/EPDM/MWCNT and **b**) vulcanized PP/EPDM/MWCNT.

Fig. 14: SEM micrographs of the fracture surface of EWF-test specimens. **a**, **b**) un-vulcanized PP/EPDM/MWCNT, **c**, **d**) vulcanized PP/EPDM/MWCNT and **e**, **f**) un-vulcanized PP/EPDM/MWCNT/PP-g-MA and **g**, **h**) vulcanized PP/EPDM/MWCNT/PP-g-MA under EWF test at two magnifications.

Fig. 15: SEM micrographs of the fracture surface of EWF-test specimens. **a**) un-vulcanized PP/EPDM/MWCNT and **b**, **c**) vulcanized PP/EPDM/MWCNT. Individual MWCNTs are shown by arrows and MWCNT aggregate is marked by dotted circle in (**a**).

Fig. 16: SEM micrographs taken from sub-surface region of EWF-test specimen for un-vulcanized PP/EPDM/MWCNT with different magnifications.

Table captions

Table I: The essential (w_e) and non-essential (βw_p) work of fracture for PP, PP/PP-g-MA and related nanocomposites (R^2 for all the samples are higher than 0.93).

Table II: The results of essential and nonessential work of fracture and splitting the essential and non-essential work of fracture into yielding and necking and tearing for all the blends and blend-nanocomposites (R^2 for all the samples are higher than 0.97).

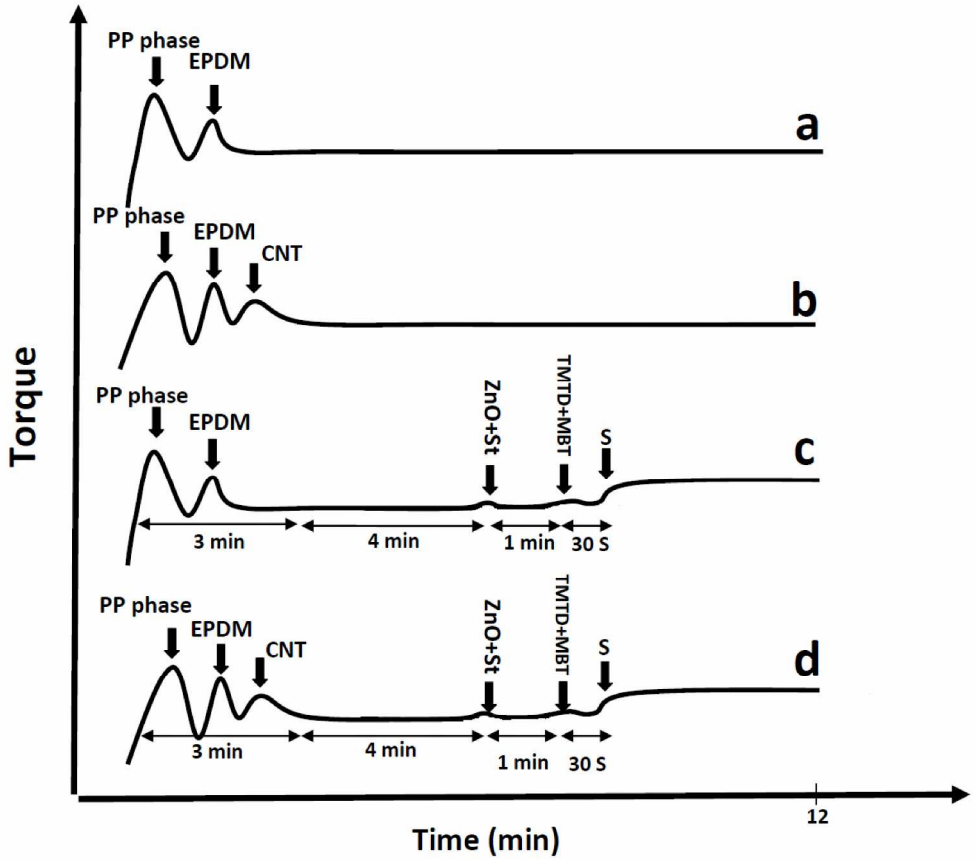

Fig. 1: Schematic mixing torque-time diagrams of un-vulcanized blend and blend nanocomposite (a and b) and vulcanized blend and blend nanocomposite (c and d).
283x251mm (300 x 300 DPI)

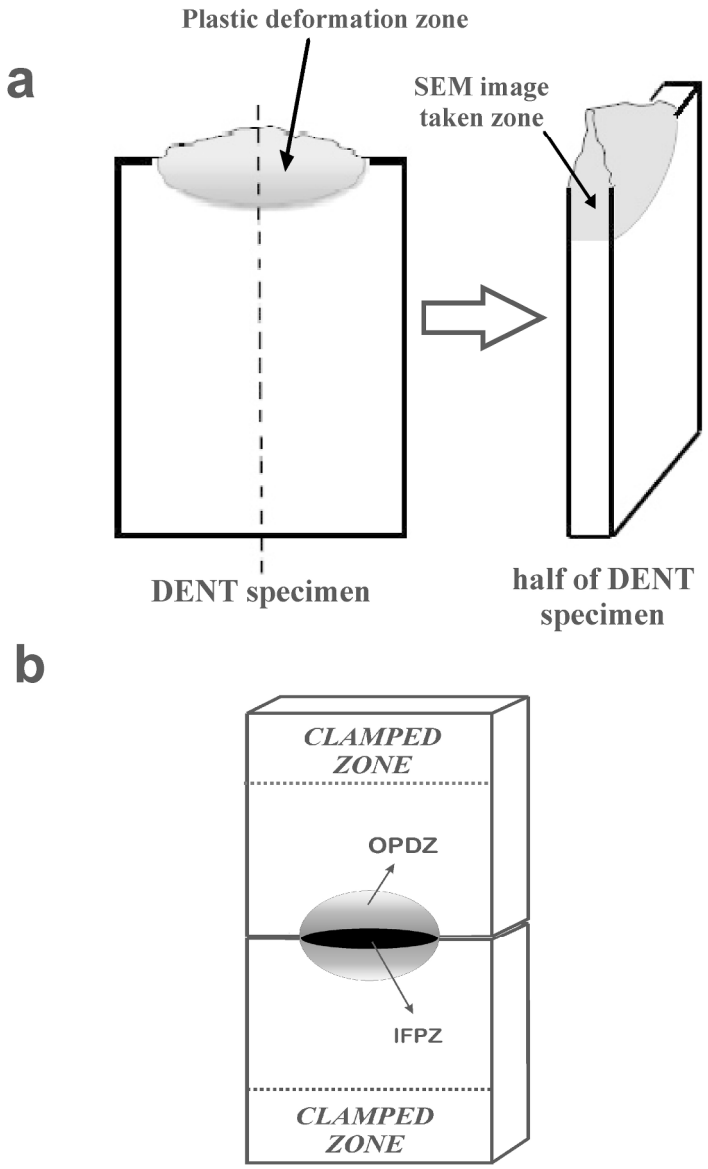

Fig. 2: a) Locations inside the plastic deformation zone that observed by scanning electron microscopy, b) Deeply double-edge notched specimen and the different energy dissipation zones involved.
186x309mm (300 x 300 DPI)

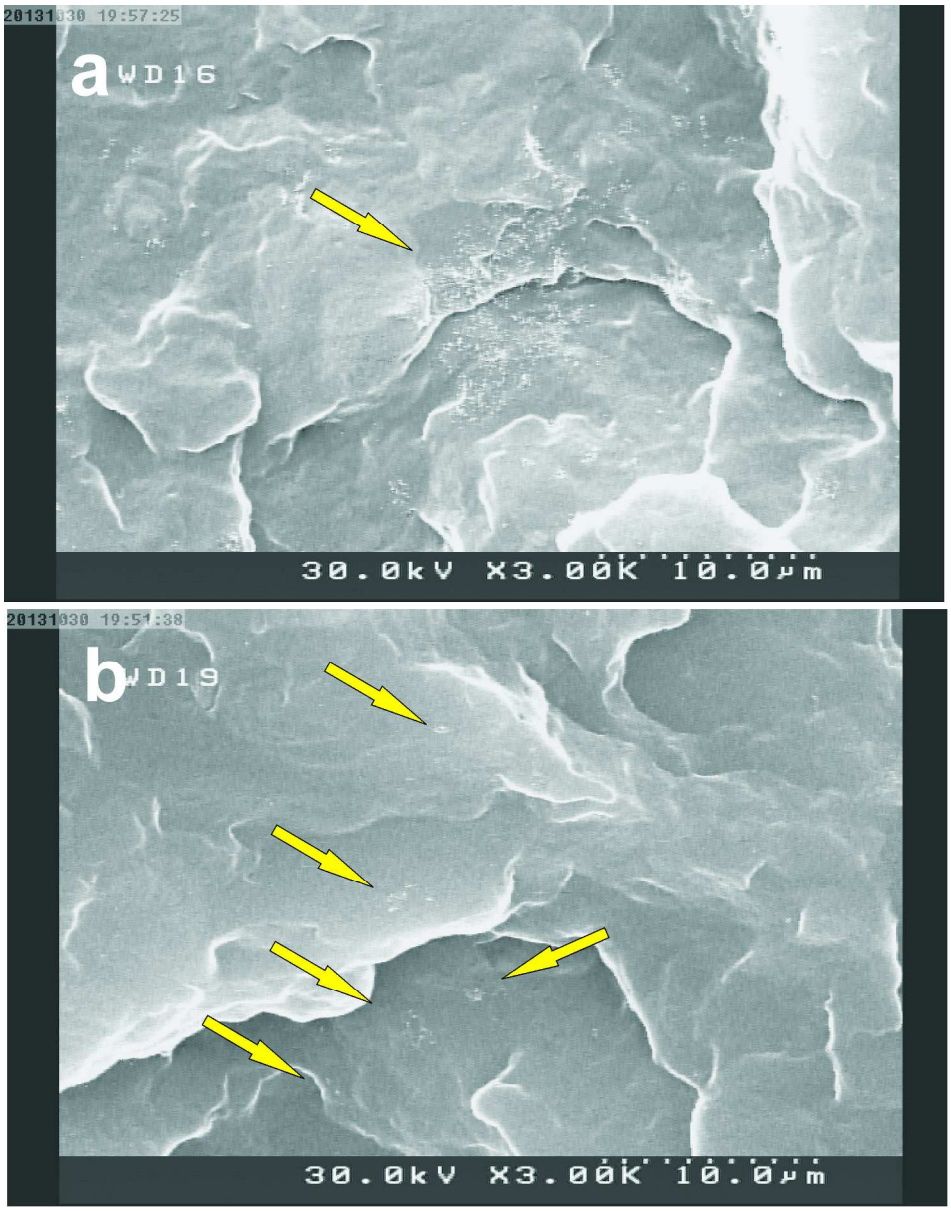

Fig. 3: SEM micrographs of a) PP/MWCNT, b) PP/MWCNT/PP-g-MA. MWCNT aggregates are shown by arrows.
208x265mm (300 x 300 DPI)

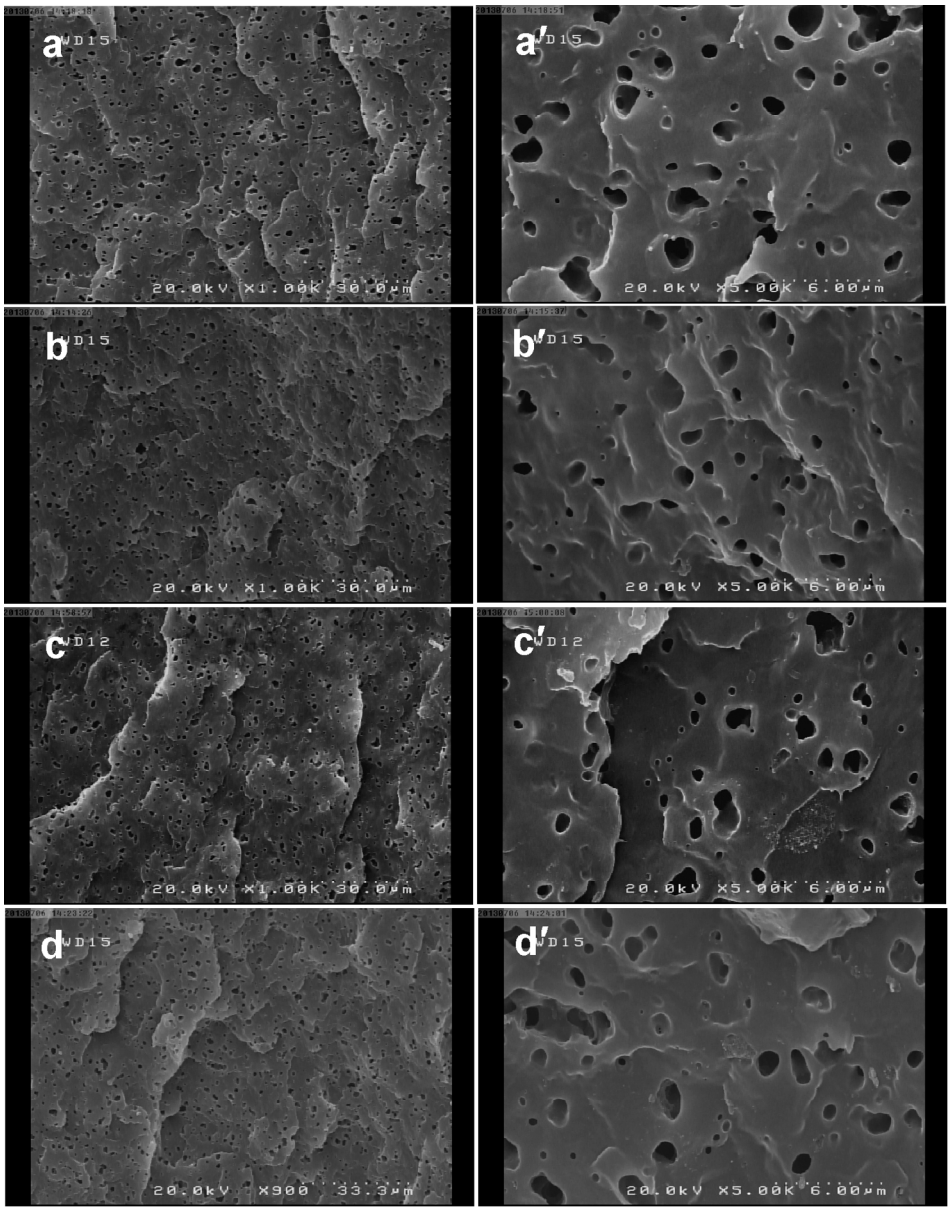

Fig. 4: SEM micrographs of different samples. a,a′) un-vulcanized PP/EPDM, b,b′) un-vulcanized PP/EPDM/PP-g-MA, c,c′) un-vulcanized PP/EPDM/MWCNT and d,d′) un-vulcanized PP/EPDM/PP-g-MA/MWCNT. The EPDM phase was etched by cyclohexane.
140x178mm (300 x 300 DPI)

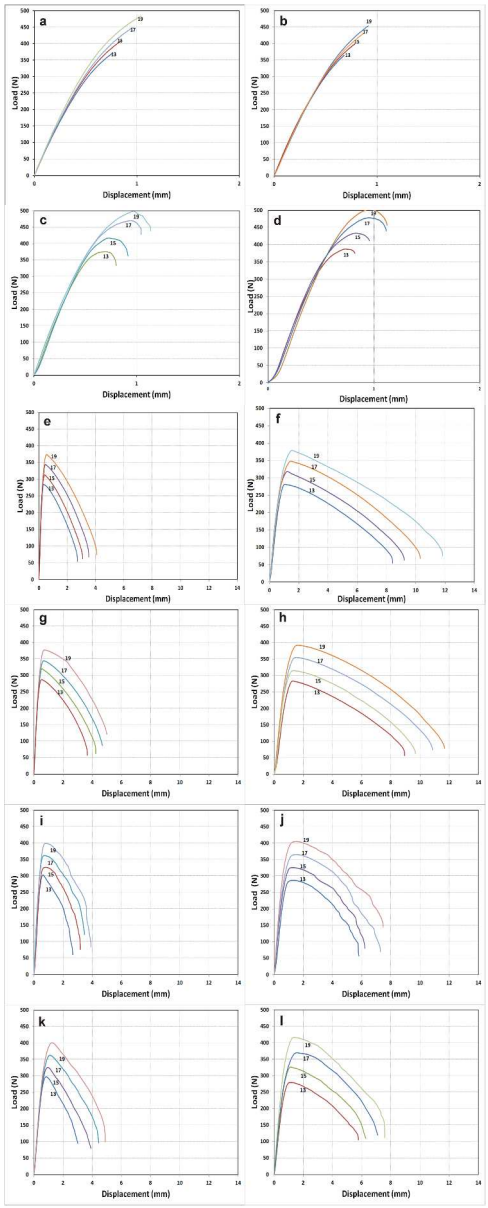

Fig. 5: Load-displacement curves of DENT specimens with different ligament lengths in EWF tests. a) PP, b) PP/PP-g-MA, c) PP/MWCNT, d) PP/PP-g-MA/MWCNT, e) un-vulcanized PP/EPDM, f) vulcanized PP/EPDM, g) un-vulcanized PP/EPDM/PP-g-MA, h) vulcanized PP/EPDM/PP-g-MA, i) un-vulcanized PP/EPDM/MWCNT, j) vulcanized PP/EPDM/MWCNT, k) un-vulcanized PP/EPDM/PP-g-MA/MWCNT and l) vulcanized PP/EPDM/PP-g-MA/MWCNT.
304x758mm (300 x 300 DPI)

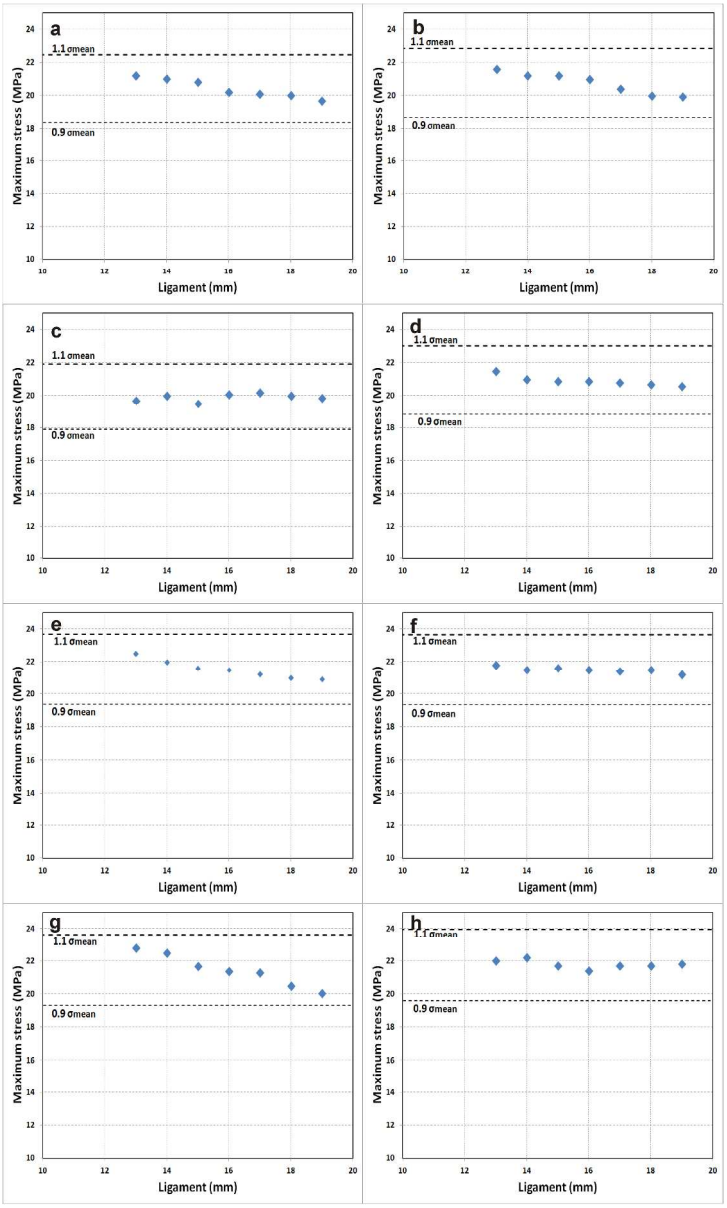

Fig. 6: maximum stress ( ) against ligament length for a) un-vulcanized PP/EPDM, b) vulcanized PP/EPDM, c) un-vulcanized PP/EPDM/PP-g-MA, d) vulcanized PP/EPDM/PP-g-MA, e) un-vulcanized PP/EPDM/MWCNT, f) vulcanized PP/EPDM/MWCNT, g) un-vulcanized PP/EPDM/PP-g-MA/MWCNT and h) vulcanized PP/EPDM/PP-g-MA/MWCNT.
304x506mm (300 x 300 DPI)

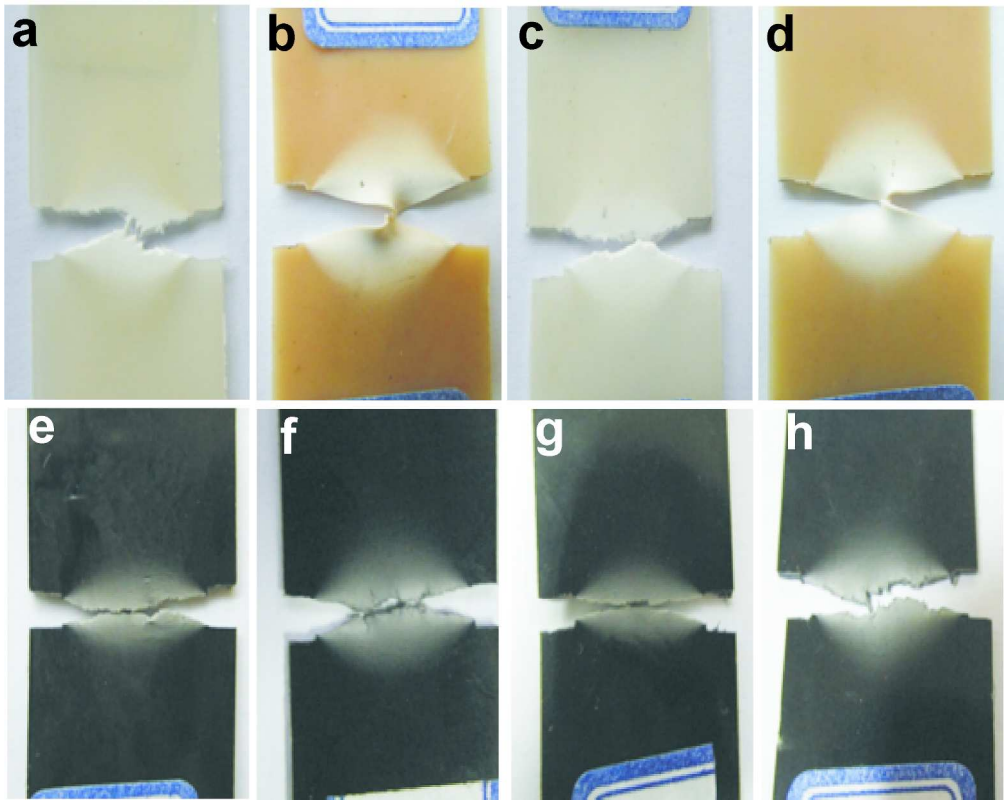

Fig. 7: Fractured DENT samples under EWF test. a) un-vulcanized PP/EPDM, b) vulcanized PP/EPDM, c) un-vulcanized PP/EPDM/PP-g-MA, d) vulcanized PP/EPDM/PP-g-MA, e) un-vulcanized PP/EPDM/MWCNT, f) vulcanized PP/EPDM/MWCNT, g) un-vulcanized PP/EPDM/PP-g-MA/MWCN and h) vulcanized PP/EPDM/PP-g-MA/MWCNT.
252x201mm (300 x 300 DPI)

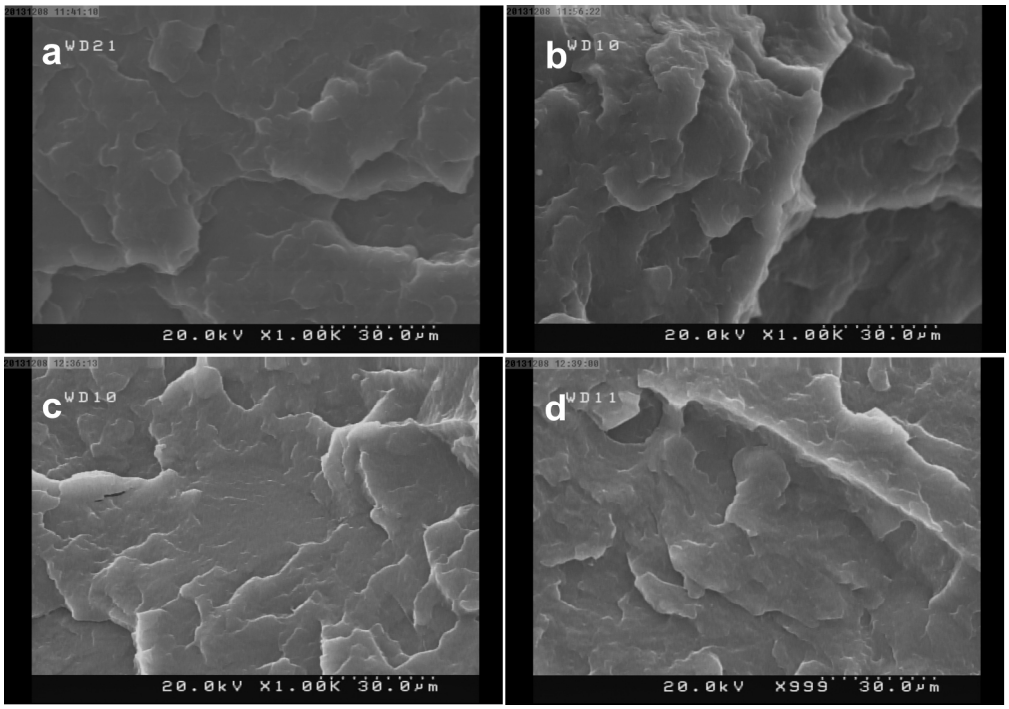

Fig. 8: SEM micrographs of the fracture surface of EWF-test specimens. a) PP, b) PP/PP-g-MA, c) PP/MWCNT and d) PP/MWCNT /PP-g-MA.
236x164mm (300 x 300 DPI)

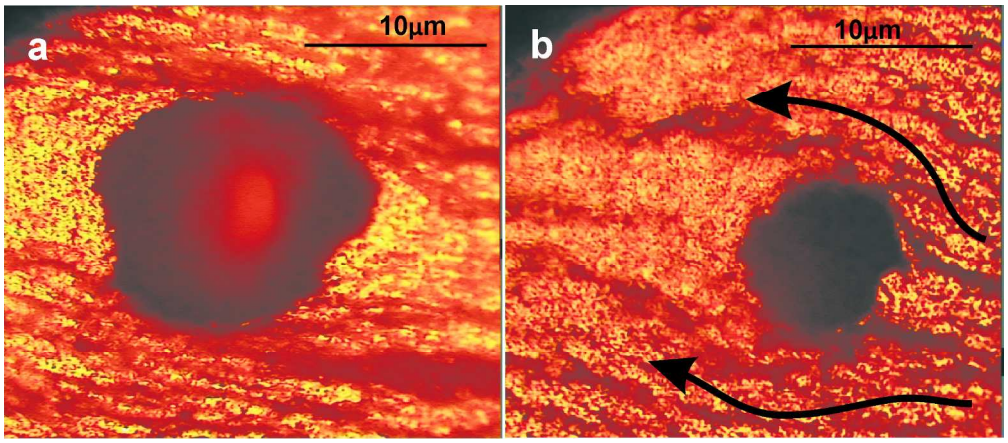

Fig. 9: Optical photomicrograph of PP/MWCNT, a) MWCNT aggregate act as craze initiation site, b) MWCNT aggregate act as crack patch hindering. The black arrows in (b) show crack path.
213x92mm (300 x 300 DPI)

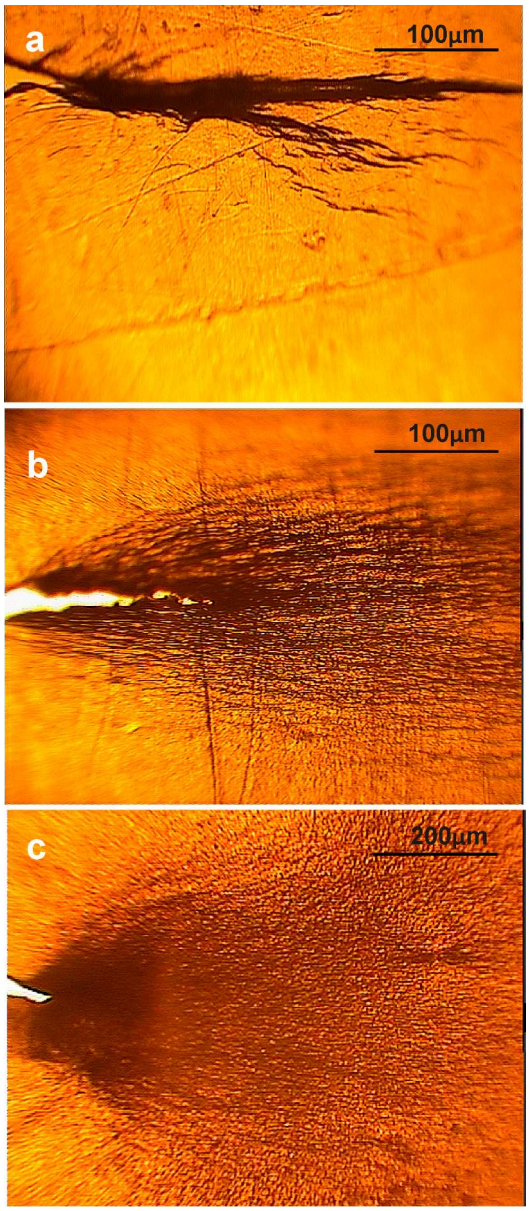

Fig. 10: Optical microscopy images of deformation zones that developed ahead of the arrested crack tip. a) PP, b) un-vulcanized PP/EPDM and c) vulcanized PP/EPDM.
117x271mm (300 x 300 DPI)

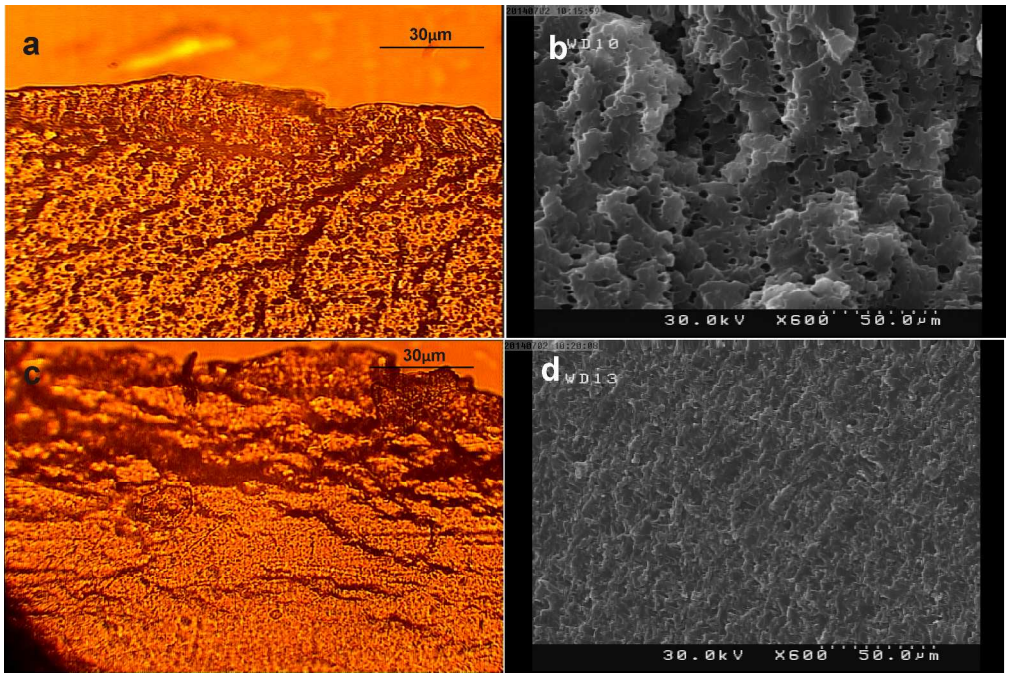

Fig. 11: Optical microscopy images of sub-surface damaged zones for un-notched films (a, c) and SEM micrographs taken from sub-surface region of EWF-test specimen (b, d). Un-vulcanized PP/EPDM (a, b) and vulcanized PP/EPDM (c, d).
254x169mm (300 x 300 DPI)

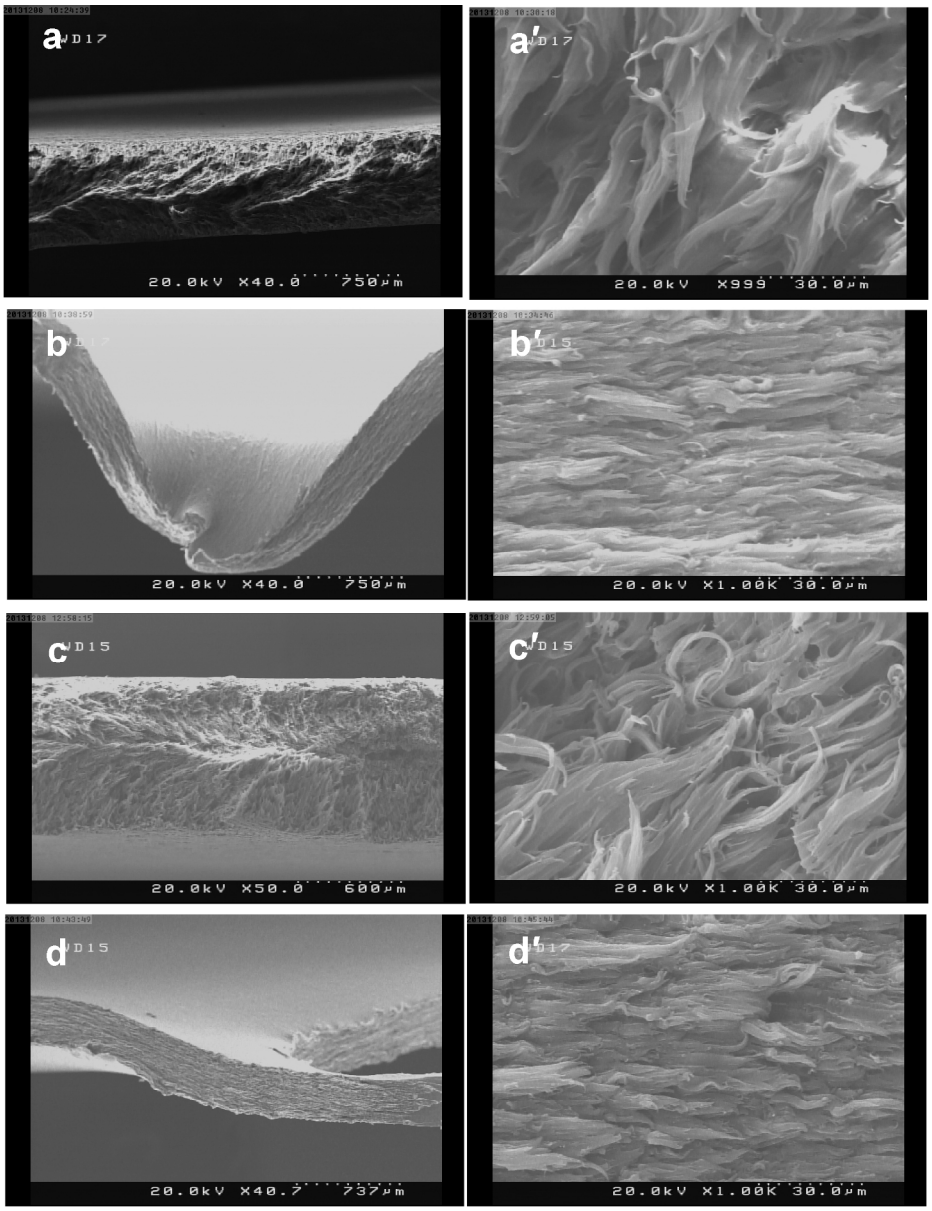

Fig. 12: SEM micrographs of the fracture surface of EWF-test specimens. a, a') un-vulcanized PP/EPDM, b, b') vulcanized PP/EPDM and c, c') un-vulcanized PP/EPDM/PP-g-MA and d, d') vulcanized PP/EPDM/PP-g-MA under EWF test at two magnifications.
209x272mm (300 x 300 DPI)

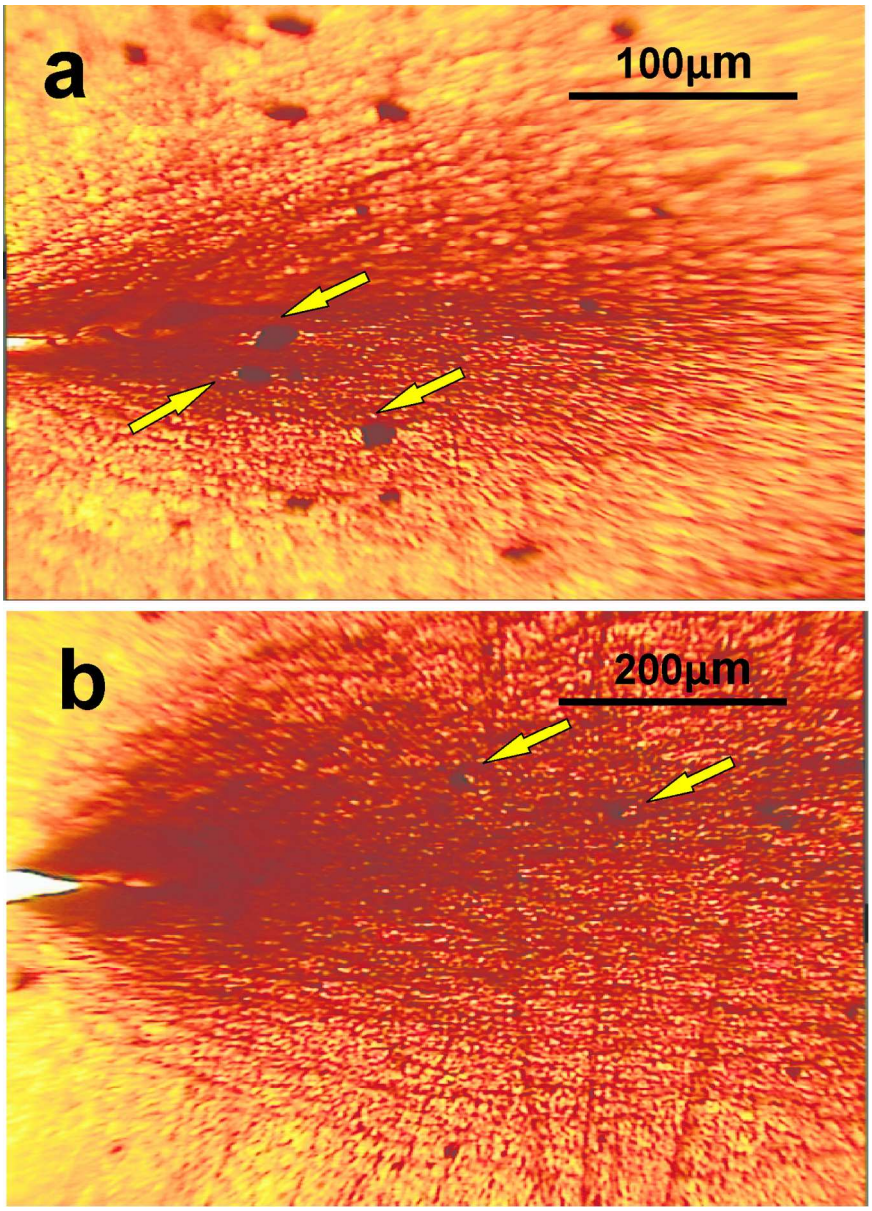

Fig. 13: Optical microscopy images of deformation zones that developed ahead of the arrested crack tip. a) un-vulcanized PP/EPDM/MWCNT and b) vulcanized PP/EPDM/MWCNT.
130x180mm (300 x 300 DPI)

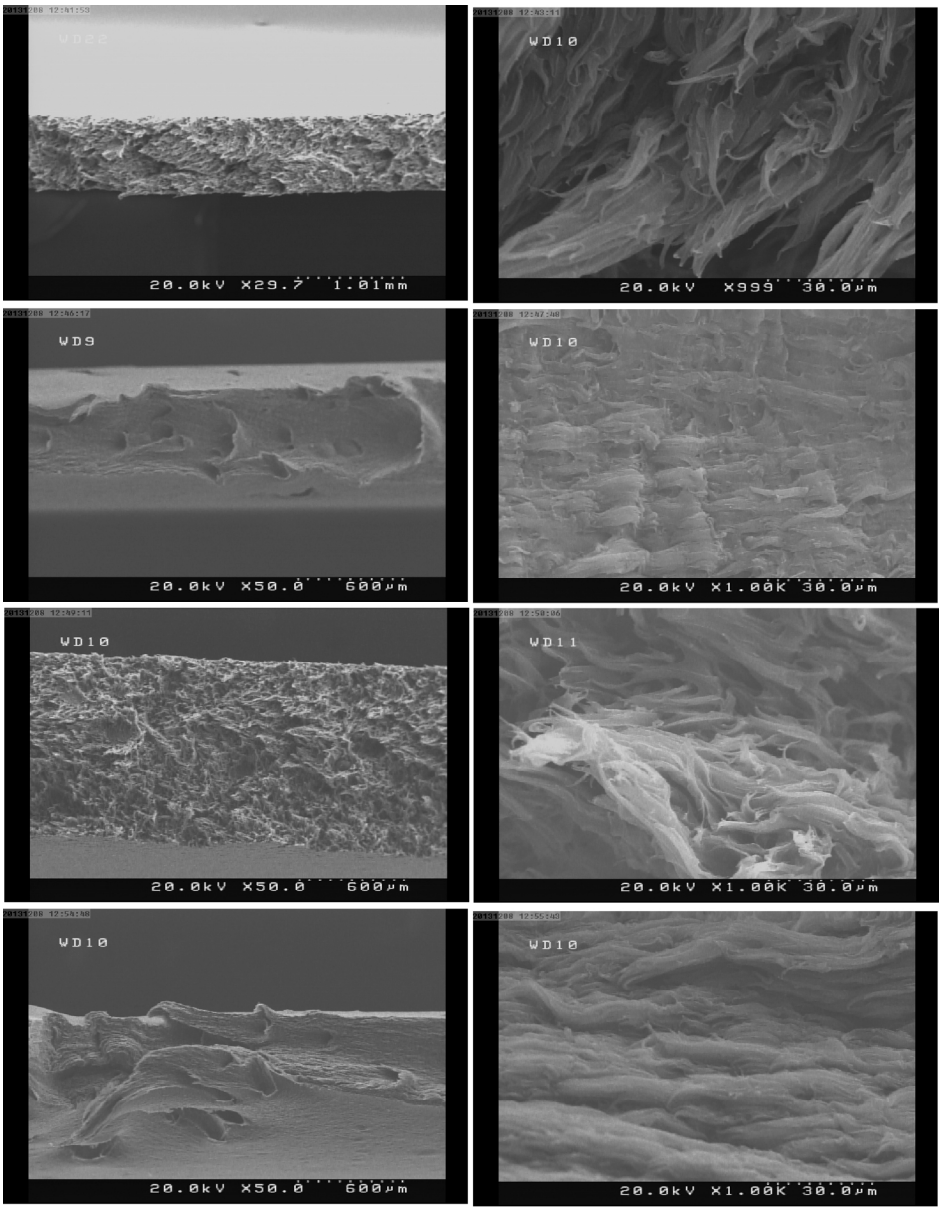

Fig. 14: SEM micrographs of the fracture surface of EWF-test specimens. a, b) un-vulcanized PP/EPDM/MWCNT, c, d) vulcanized PP/EPDM/MWCNT and e, f) un-vulcanized PP/EPDM/MWCNT/PP-g-MA and g, h) vulcanized PP/EPDM/MWCNT/PP-g-MA under EWF test at two magnifications.
167x215mm (300 x 300 DPI)

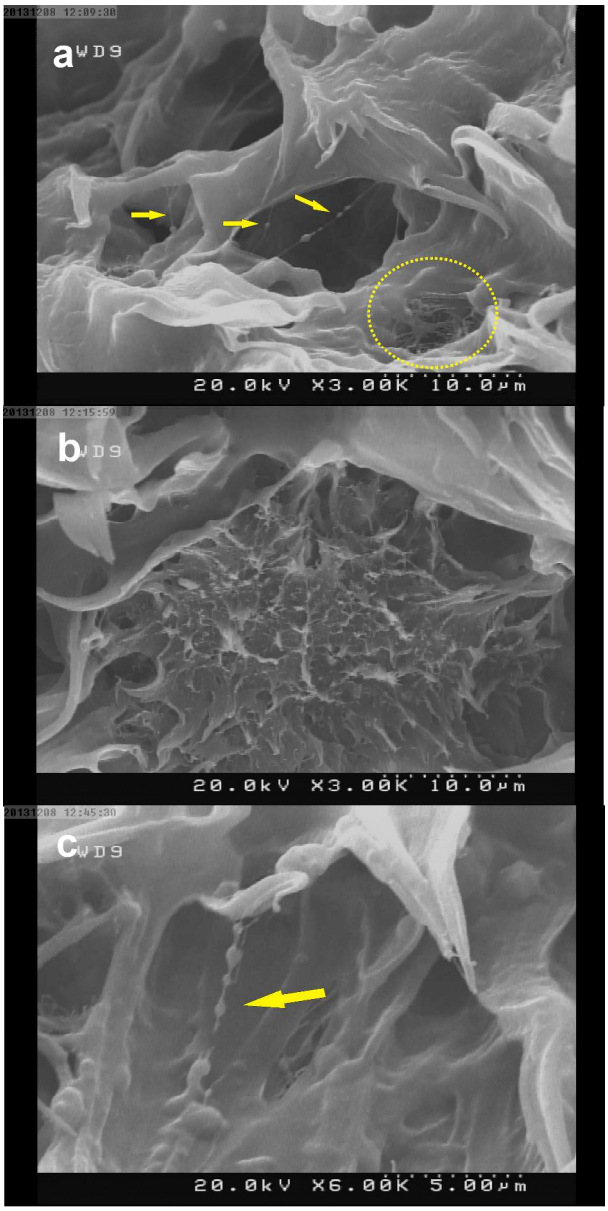

Fig. 15: SEM micrographs of the fracture surface of EWF-test specimens. a) un-vulcanized PP/EPDM/MWCNT and b, c) vulcanized PP/EPDM/MWCNT. Individual MWCNTs are shown by arrows and MWCNT aggregate is marked by dotted circle in (a).
178x355mm (300 x 300 DPI)

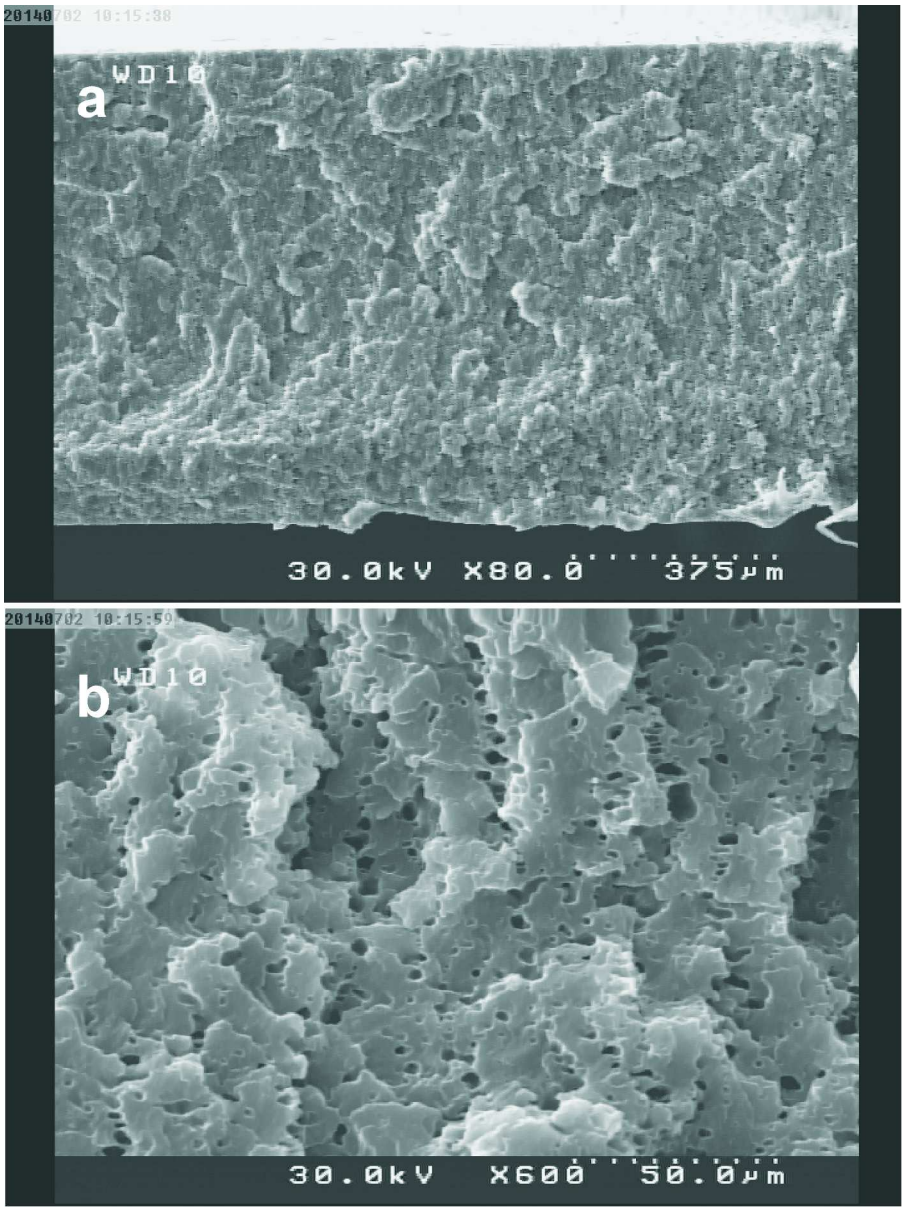

Fig. 16: SEM micrographs taken from sub-surface region of EWF-test specimen for un-vulcanized PP/EPDM/MWCNT with different magnifications.
194x260mm (300 x 300 DPI)

Table I: The essential (w_e) and non-essential (βw_p) work of fracture for PP, PP/PP-g-MA and related nanocomposites (R^2 for all the samples are higher than 0.93).

Samples	w_e N/mm	βw_p N/mm^2
PP	4.6±0.2	0.61±0.06
PP/PP-g-MA	4.5±0.2	0.51±0.05
PP/MWCNT	5.03±0.2	0.81±0.07
PP/MWCNT/PP-g-MA	5.2±0.2	0.85±0.06

Table II: The results of essential and nonessential work of fracture and splitting the essential and non-essential work of fracture into yielding and necking and tearing for all the blends and blend-nanocomposites (R^2 for all the samples are higher than 0.97).

	Samples	w_e N/mm	βw_p N/mm^2	$w_{e,y}$ N/mm	$\beta_y w_{p,y}$ N/mm^2	$w_{e,n}$ N/mm	$\beta_n w_{p,n}$ N/mm^2
un-vulcanized	PP/EPDM	9.7±0.5	2.3±0.15	1.28±0.1	0.28±0.03	8.47±0.5	2.08±0.15
	PP/EPDM/PP-g-MA	18.7±1	3±0.12	1.42±0.1	0.41±0.0.3	17.3±1	2.52±0.15
	PP/EPDM/MWCNT	7.8±0.6	2.8±0.2	2.2±0.12	0.6±0.05	5.6±0.3	2.2±0.18
	PP/EPDM/MWCNT/PP-g-MA	13.2±0.6	3.3±0.2	3.6±0.12	0.8±0.05	9.6±0.5	2.5±0.2
vulcanized	PP/EPDM	47.3±2	5±0.2	3.8±0.2	0.89±0.05	43.5±2	4.1±0.25
	PP/EPDM/PP-g-MA	50.8±2	5.2±0.25	4.2±0.23	0.98±0.05	46.6±2	4.2±0.25
	PP/EPDM/MWCNT	30.5±2	5.4±0.3	4.8±0.25	1.1±0.06	25.7 ±2	4.3±0.3
	PP/EPDM/MWCNT/PP-g-MA	32.5±2.5	5.6±0.3	5.89±0.3	1.2±0.06	26.6 ±2.5	4.4±0.3